ACS APPLIED NANO MATERIALS

Article

Safe-by-Design Flame Spray Pyrolysis of SiO$_2$ Nanostructures for Minimizing Acute Toxicity

Fotini Fragou, Panagiota Stathi, Yiannis Deligiannakis,* and Maria Louloudi*

Cite This: https://doi.org/10.1021/acsanm.2c01273

Read Online

ACCESS | Metrics & More | Article Recommendations | Supporting Information

ABSTRACT: Reactive oxygen species (ROS) generation is considered as a critical factor in nanosilica's cell toxicity. Herein, we present a method for controlling the ROS generation by nanosilica toward designing safer-to-use nanosilica materials with minimal acute toxicity. The present work demonstrates a one-step process to synthesize nanosilica materials with minimal ROS production, using the flame spray pyrolysis (FSP) technology, which is currently used for industrial production of SiO$_2$. We show that controlling the temperature regime of nano-SiO$_2$ synthesis in the FSP process allows passivation of the nanosilica surface and, subsequently, control of the ROS production capacity. In this context, using FSP, we have engineered *in situ* three types of nanosilica materials produced either under high-temperature combustion (ordinarily fumed SiO$_2$) or low-temperature combustion (rSiO$_2$) as well as their combination in a core−shell configuration (rSiO$_2$@SiO$_2$). Electron paramagnetic resonance and Raman spectroscopies were used to study the correlation between ROS formation and the structure of siloxane rings of the silica network. In parallel, the acute toxicity of the particles was monitored by Microtox (*Aliivibrio fischeri*). Our data show that the acute toxicity and ROS are both correlated with the FSP temperature regime according to the sequence SiO$_2$ ≫ rSiO$_2$@SiO$_2$ > rSiO$_2$. A comprehensive physicochemical mechanism is discussed, which relates the surface-ring structure of nano-SiO$_2$ with ROS yield and acute toxicity. The present findings and the FSP methodology provide a more general easy-to-apply road map for safe-by-design production of metal oxides for issues related to ROS toxicity.

KEYWORDS: nanosilica, flame spray pyrolysis, reactive oxygen species, EPR spectroscopy, nanotoxicity, silica passivation, Microtox, Aliivibrio fischeri
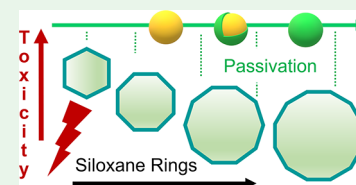
1. INTRODUCTION

Silicon dioxide nanomaterials, commonly called nanosilica, hold a critical position among the engineered nanomaterials due to their intrinsic physicochemical characteristics, i.e., surface charge and reactive surface species.[1,2] Nanosilica can be crystalline and noncrystalline (amorphous), and its structure may involve siloxane ring bridges (≡Si−O−Si≡) and terminal silanols [≡Si−OH and =Si(OH)$_2$].[3,4] The siloxane bridges occur either as small three-membered rings (3MRs) that form predominantly under high-temperature synthetic procedures or larger rings, e.g., four-membered rings (4MRs), five-membered rings (5MRs), and six-membered rings (6MRs) as specified by Zhang *et al.*[5] A 3MR is composed of three Si atoms conjoined by three oxygen atoms. Amorphous nanosilica is produced in tons per year through two main synthesis technologies: [i] by molecular condensation of silanol groups in aqueous solutions or [ii] by flame synthesis, e.g., by Evonik, which utilizes flame spray pyrolysis (FSP) synthesis.[5]

FSP technology is currently widely used as an industrial-scale technology for nanomaterials manufacturing.[6−9] FSP allows control of the physicochemical and structural characteristics of the produced nanomaterials on demand[10,11] *via* control of the process. Thus, high-purity and controlled-composition materials can be produced even for bioapplications.[12] So far, however, there is converging evidence that fumed nanosilica, including FSP-made, can exhibit non-negligible cell toxicity.[13−16]

Although thoroughly studied *in vivo*, *in vitro*, and *in silico*, the toxicity of nanosilica remains a complex phenomenon until today.[3,4] It is known that crystalline forms of silica exhibit toxicity: cristobalite, opal, or tridymite cause toxic side effects, mainly due to morphological characteristics.[17] Pavan *et al.*, in a recent study concerning nanosilica crystallinity, have observed that nearly free silanols can damage cellular membranes and initiate inflammatory reactions.[4] By studying the toxicity induced by nearly free silanols, their concentration and chemical origin should be evaluated.[18] However, noncrystalline silica, composed mainly of an amorphous matrix, possesses a different and more complex toxicity profile. Moreover, there are inconsistencies in the literature concerning each physicochemical characteristic of the engineered amorphous nanosilica in relation to toxicity effects. However, in all cases, the generation of reactive oxygen species (ROS) can be a

A

common factor in many adverse effects of amorphous nanosilica.[19,20] A recent study proposed a direct connection of cellular toxicity with nanoparticle-generated ROS.[21]

In nature, ROS are chemically reactive species produced in the cells, i.e., as a byproduct of normal oxygen metabolism. They may play critical roles in living organisms as they can facilitate cellular signaling pathways[19] and oxidative stress, resulting in physiological redox-regulated dysfunction and ensuing physio-pathological damage, including genotoxicity, inflammation, or carcinogenesis.[19,22] In this context, comprehension of the mechanisms of ROS generation by nanosilica, their control, and minimization is a key challenge. Ideally, designing effective nanosilica synthesis methods for eliminating ROS generation is a desirable safe-by-design strategy.

ROS include singlet oxygen ($^1O_2$), the superoxide anion radical ($^\bullet O_2^-$), and hydroxyl radicals ($^\bullet OH$).[23] In the case of nanosilica, hydroxyl radical ($^\bullet OH$) generation is a common phenomenon.[5,21,23] Hydroxyl radicals endanger the biological processes of the cells since they possess the highest one-electron redox potential of all the relevant ROS.[24,25] Herein, our main hypothesis was that $^\bullet OH$ generation is the crucial factor determining the ROS-related toxicity of FSP-made nanosilica particles. Currently, there are different theories concerning ROS production mechanisms by nanosilica. Zhang *et al.*[5] suggested that the strain of 3MRs enhances the formation of surface $^\bullet OH$ radicals *via* homolytic cleavage of Si−O−Si bonds. Many research teams stated that the silanol groups on the surface determine the surface chemistry and influence the overall ROS production.[3,18,24] Additionally, the aggregation size and surface charge are two factors that may facilitate the ROS generation capacity of nanosilica materials.[26,27]

The present study proposes a novel synthesis strategy to control ROS generation by FSP nanosilica toward minimal acute toxicity. Our focus was on passivating the strained siloxane matrix to a more "relaxed" one, focusing on the siloxane rings, and studying the effect of passivation on the ROS generation capacity. Two different passivation methods were developed and validated herein: [i] an *in situ* FSP passivation and [ii] a post-FSP passivation. Concurrently, a detailed physicochemical characterization was carried out that allowed us to parametrize ROS generation by FSP nanosilica and achieve minimal acute toxicity.

The concept behind our FSP passivation consists primarily of altering the surface chemistry of nanosilica by lowering the temperature of the FSP synthesis through an alternative configuration of the FSP reactor setup. The impact of a lower flame temperature, and different flame residence times, on SiO_2, has been previously studied.[28] Thus, our specific aims were [i] to design and test an FSP setup that allows the production of SiO_2 at a high- or low-T regime, [ii] to produce high-T SiO_2, herein codenamed SiO_2, low-T SiO_2, herein codenamed $rSiO_2$, and low-T SiO_2 coating on high-T SiO_2, herein codenamed $rSiO_2@SiO_2$, [iii] to monitor the ROS generation by the nanosilica materials using electron paramagnetic resonance[29] spectroscopy, [iv] to evaluate the acute toxicity of the FSP-made nanosilica materials on *Aliivibrio fischeri*, and finally, [v] to discuss the comprehensive mechanism regarding the correlation between ROS toxicity and the FSP process.

2. EXPERIMENTAL SECTION

2.1. Reagents and Solvents. HMDSO (purity, 98%), xylene (>97%), hydrogen peroxide (30% aqueous solution), KBr (spectroscopic grade), ethanol (analytical grade), 5,5-dimethyl-1-pyrroline *N*-oxide (DMPO), NaOH (analytical grade), HNO$_3$ (analytical grade), and buffers *N*-(2-hydroxyethyl)piperazine-*N'*-(2-ethane sulfonic acid) (HEPES) and 4-morpholineethanesulfonic acid (MES hydrate) were purchased from Merck and Aldrich. 2,2-Diphenyl-1-picrylhydrazyl (DPPH) was obtained from Sigma-Aldrich and used within one month of its purchase. O$_2$ gas (purity, >99%), N$_2$ gas (purity, >99%), and CH$_4$ gas (purity, >99%) were purchased from Linde. Aerosil A90 nanosilica was purchased from Evonik. Ultrapure water was provided by a Milli-Q system (Millipore).

2.2. Instrumentation. FT-IR spectra were recorded on a Thermo Scientific Nicolet iS5 FT-IR spectrometer within 400−4000 cm^{-1}. The spectra of the dried samples were obtained in KBr pellets (Merck, spectroscopic grade).

Raman spectra were recorded with a HORIBA-Xplora Plus instrument coupled to an Olympus BX41 microscope, equipped with a 785 nm diode laser as an excitation source. The spectra were recorded for 10 s with 10 accumulations to obtain a good signal-to-noise ratio.

The specific surface area (SSA) and the pore size distribution of the samples were determined from N$_2$ adsorption desorption isotherms. The N$_2$ adsorption/desorption isotherms were measured at 77 K on a Quantachrome NOVAtouch LX2. The samples were outgassed at 150 °C for 16 h under a vacuum before the measurements. The specific surface area (SSA) was determined using adsorption and desorption data points with the Brunauer−Emmett−Teller (BET) method. The specific surface area (S_{BET}) was found using adsorption data points in the relative pressure P/P_o range of 0.1−0.3. Meanwhile, the BJH method was used for the pore radius using the absorption data points from 0.35−0.99 P/P_o, and the total pore volume was obtained at the 0.99 P/P_o points.

2.2.1. Radical Monitoring by Electron Paramagnetic Resonance (EPR). EPR spectra were recorded with a Bruker ER200D spectrometer at room temperature, equipped with an Agilent 5310A frequency counter. An adequate signal-to-noise ratio was obtained after 16 scans. Spin quantitation was done using DPPH as the spin standard. DPPH is a stable radical used widely as an EPR quantification standard, and its spectrum is a singlet signal (g = 20,036). EPR signals are generated by half-integer spin moieties, which are the $^\bullet OH$ radicals in the present work. However, as $^\bullet OH$ radicals are very short-lived, we utilize DMPO (5,5-dimethyl-1-pyrroline *N*-oxide) to monitor hydroxyl radical generation.[30] All EPR experiments were carried out at least three times.

Size and surface charge measurements were obtained using a HORIBA nanoPartica analyzer SZ-100. T*o* choose the optimal sample concentration for the size analysis, a series of measurements in different concentrations were carried out. A plot of the measured size data as a function of concentration is shown in Figure S1 in the Supporting Information. The error bars show the standard deviation of repeated measurements. Considering those results, dispersions of the nanomaterials in Milli-Q water at a concentration of 1 mg/10 mL were measured for size after mild sonication (20 W) for 5 min.

Regarding the zeta potential measurements, dispersions of 4 mg/160 mL were prepared. The dispersion was (a) sonicated (20 W) for 15 min at 35 °C and (b) degassed for 15 min before titration using N$_2$ gas. HNO$_3$ (0.1 M) and NaOH (0.1 M) were used as titrants. Dehydration of rSiO$_2$-p was achieved by mildly heating (40 °C) under a vacuum for 24 h. Hydration in the case of the rSiO$_2$ nanosilica material was achieved by placing the material in a desiccator that contained distilled water under a vacuum for 48 h.

The material morphology was analyzed by high-resolution transmission electron microscopy (HRTEM) using a Philips CM 20 microscope operated at 200 kV and providing a 0.25 nm resolution. Before the measurements, the samples were ground in a mortar and dry-loaded onto a support film (lacey carbon, 300 mesh, Cu). Recorded pictures were analyzed by Gatan Digital Micrograph
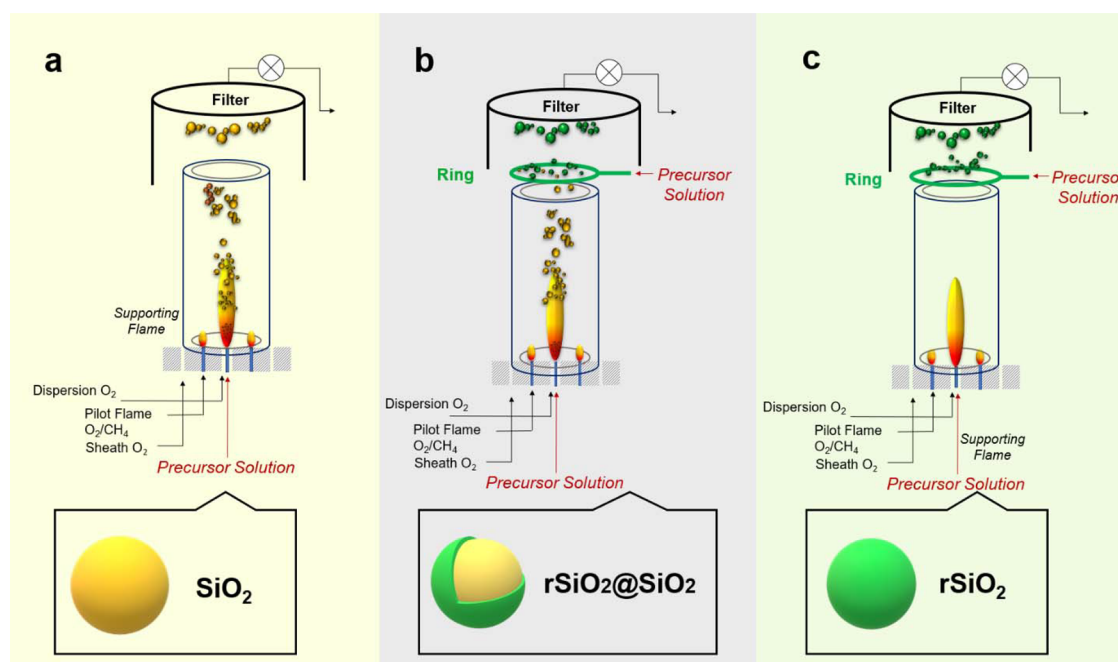
Figure 1. Schematic representation of our flame spray pyrolysis reactor setup (a) for the high-temperature nano-SiO_2, (b) for the hybrid $rSiO_2@SiO_2$ nanosilica, and (c) for the low-temperature nano-$rSiO_2$.

software. The particle size and thickness of the SiO_2 layer were calculated using ImageJ software.

2.2.2. Microtox Tests. A Microtox LX analyzer by Modern Water was used to provide acute toxicity information of the SiO_2 NPs through bioluminescence quantification of the bacterial strain *Vibrio fischeri*. The bacterial cultures were exposed to NPs with an initial concentration of 495 mg/L for 15 min, and their luminescence intensity was measured. Before use, the NPs were dispersed by mild sonication (20 W) for 5 min. The effective NP concentration in which a 50% decrease in luminescence intensity (EC_{50}) was induced was calculated by linear regression. Zinc sulfate was studied as a positive toxicity control.

2.3. Materials Synthesis. *2.3.1. SiO₂ Nanoparticle Synthesis by FSP. 2.3.1.1. FSP Process Setup.* Our single-nozzle FSP reactor setup was described in detail previously.[31] The three types of silica nanoparticles, SiO_2, $rSiO_2@SiO_2$, and $rSiO_2$, were prepared *via* three different configurations of the FSP reactor, see Figure 1. This commonly used FSP setup results in high-temperature SiO_2, i.e., injecting and combusting the liquid HMDSO precursor *via* the flame (Figure 1a).[5] The low-temperature silica $rSiO_2$ was prepared by injecting the liquid HMDSO precursor at a distance above the flame (see Figure 1c) *via* an injection ring. The ring injection method was previously developed by Pratsinis' group[32,33] and successfully used to coat FSP-made particles, e.g., TiO_2, with SiO_2 nanolayers. In our FSP-ring setup (Figure 1c), the flame was generated by combusting a high-enthalpy solvent (xylene) without any metal precursor. Thus, the combustion flame provides only an upward thermal field. At the same time, the Si precursor (HMDSO) was sprayed *via* the ring at a height above the flame, see Figure 1, where the temperature was significantly lower. This resulted in low-T (<600 °C) combustion of HMDSO that provided the $rSiO_2$ collected in a glass-fiber FSP filter. Lastly, a mixed, core–shell-type nanosilica hybrid was produced by combining processes (a) and (c), i.e., ring injection of HMDSO on the flame-produced stream of SiO_2 particles (Figure 1b) producing the hybrid $rSiO_2@SiO_2$ material. In this configuration, we achieved $rSiO_2@SiO_2$ nanosilica composed of a SiO_2 core coated by an $rSiO_2$ shell, as depicted in Figure 1b.

2.3.1.2. High-Temperature SiO₂. A high-temperature flame was used to engineer flame SiO_2 (Figure 1a). The precursor solution was prepared by dissolving 0.5 M HMDSO (hexamethyldisiloxane) in ethanol. Then, the solution was fed through a capillary at 5.0 mL/min

and dispersed by 5.0 L/min O_2 (Linde; purity, >99%) to a stoichiometric, self-sustained oxygen–methane (5.0 and 2.5 L/min) pilot flame to start combustion, resulting in the formation of the nanoparticles. The pressure drop at the nozzle tip was fixed at 2.0 bar, and an added 5.0 L/min sheath O_2 was used. Using a vacuum pump (Busch V40), the powder product was collected on a glass microfiber filter.

The combustion enthalpy was calculated based on eq 1 described previously by Jossen *et al.*[34] and others.[24,28]

$$\frac{\text{combustion enthalpy}}{\text{total inlet mass flow}}$$

$$= -\frac{\Delta n_{\text{prec}/\Delta t}\Delta H_c^{\text{Prec}} + \Delta n_{\text{solv}}/\Delta t \Delta H_c^{\text{Solv}} + \Delta n_{\text{CH4}/\Delta t}\Delta H_c^{\text{CH4}}}{\Delta m_{\text{prec}}/\Delta t + \Delta m_{\text{disp-O2}}/\Delta t + \dot{m}_{\text{CH4-flame}} + \Delta m_{\text{O2-flame}/\Delta t}}$$

(1)

In eq 1, $\Delta n/\Delta t$ and $\Delta m/\Delta t$ stand for the inlet flow rate in mol/min and kg/min, respectively, and ΔH_c (MJ/mol) is the combustion enthalpy of each component, considering the total combustion of the component and enthalpy of product formation. Herein, for the nanoparticle produced by our "hot flame" using 0.64 M precursor HMDSO and a feed ratio of 5.0 mL/min, the calculated combustion enthalpy was 9.2 MJ/min. We clarify that the term "high-temperature SiO_2" that we use herein refers relatively to our ring-sprayed "low-temperature" SiO_2. In the work of Spyrogianni *et al.*, the terms "hot" and "cold" were used to distinguish SiO_2 particles made by FSP under total combustion enthalpy of >15 MJ/kg vs <11 MJ/kg, respectively,[28] produced by varying the precursor-to-dispersion oxygen flows.

2.3.1.3. Low-Temperature rSiO₂ and rSiO₂@SiO₂. The coating of SiO_2 NPs with SiO_2 was engineered in a modified enclosed FSP reactor, initially described by Sotiriou *et al.*[11,32,33,35,36] Flames were enclosed by a 22.0 cm-long metallic tube, schematically shown in Figure 1b with a metal spraying ring at the top. Our spraying ring (diameter = 4.3 cm) had 12 equidistant holes of a 500 μm diameter, each directed away from the centerline of the ring and pointing upstream to avoid stagnation of flow. A gas stream carrying the Si precursor (HMDSO, Aldrich, 98%) was injected through these openings. This stream was further conveyed to the spraying ring using

266 an additional N_2 stream, with a flow rate of 15.0 L/min N_2 at room
267 temperature. In this setup, the HMDSO vapor was conveyed by
268 bubbling N_2 gas through a glass flask (3.0 L/min N_2 (Linde; purity,
269 >99%)) containing an HMDSO:ethanol mixture (70:30 v:v),
270 according to the method by Teleki et al.[32,37] and our previous
271 work.[11] To produce $rSiO_2$ via the spraying ring, the same spraying
272 ring FSP setup was used. In this case, the FSP flame was created by
273 the combustion of xylene alone, fed through the FSP nozzle capillary.
274   To calculate the combustion enthalpy of the "low-temperature
275 particles", the concentration of the Si precursor feed ratio via the ring
276 was calculated theoretically using the Antoine equation, according to
277 Teleki et al.[32,37] for SiO_2 coatings by FSP. The so-called Antoine
278 equation (eq 2) describes the relation between vapor pressure and
279 temperature for pure substances:[38]

280 $$\log_{10}(P) = A - [B/(T + C)] \qquad (2)$$

281 where P is the calculated vapor pressure (bar) and T is the
282 temperature in Kelvin. Using the reference values for A, B, and C for
283 our Si precursor as listed in the handbook of Yaws,[38] we estimated the
284 vapor pressure according to eq 2. Using the ideal gas law,[32,37] the P of
285 HMDSO was converted to mol of HMDSO. Then, using eq 1, the
286 combustion enthalpy was calculated to be 6.8 MJ/mol.
287   Here, we assumed that for the high-T configuration (Figure 1a),
288 silica particle formation occurs in the gas phase at T in the range of
289 1800−2500 K, as the precursor fully evaporates and forms product
290 particles by chemical reaction, coagulation, and sintering.[11,31,32] In the
291 case of ring-sprayed particles, see Figure 1c, the temperature was
292 lowered significantly, i.e., it was measured by a probe to be in the
293 range of 700−900 K. Apart from the typical thermal dissipation, the Si
294 carrier N_2 gas contributed to the cooling.
295   *2.3.2. Post-FSP Passivation of SiO₂.* To further investigate the
296 surface properties and the role of the siloxane rings in ROS
297 generation, we have developed a post-FSP treatment protocol to
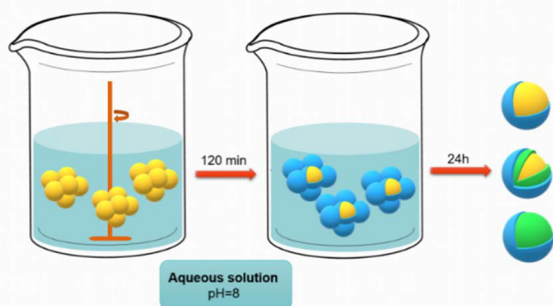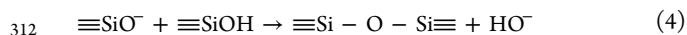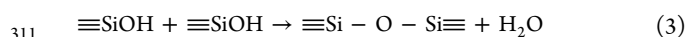298 passivate the silica surface, as depicted schematically in Figure 2. Our

Figure 2. Schematic representation of the post-FSP alkaline treatment protocol.

299 specific hypothesis was that we could passivate the SiO_2 surface using
300 a sol−gel-type chemical treatment to promote the condensation of the
301 surface silanol groups according to the fundamental polycondensation
302 reactions 3 and 4.[39] In this way, larger siloxane rings would form on
303 the surface, leading to a more "relaxed" and, therefore, less reactive
304 nanosilica surface. In this context, aqueous suspensions of the
305 nanomaterials (2.0 g/L) were first stirred for 120 min at pH = 8.0
306 (stabilized with an MES (10 mM)−HEPES (10 mM) buffer
307 solution). The obtained nanomaterials were thoroughly washed
308 with water (pH = 7.0) and freeze-dried overnight. The final materials
309 were coded as SiO_2-p, $rSiO_2@SiO_2$-p, and $rSiO_2$-p ("p" stands for
310 post-treatment).

311 $$\equiv SiOH + \equiv SiOH \rightarrow \equiv Si - O - Si\equiv + H_2O \qquad (3)$$

312 $$\equiv SiO^- + \equiv SiOH \rightarrow \equiv Si - O - Si\equiv + HO^- \qquad (4)$$

3. RESULTS AND DISCUSSION

     3.1. Particle Morphology. The TEM images of the SiO_2 313
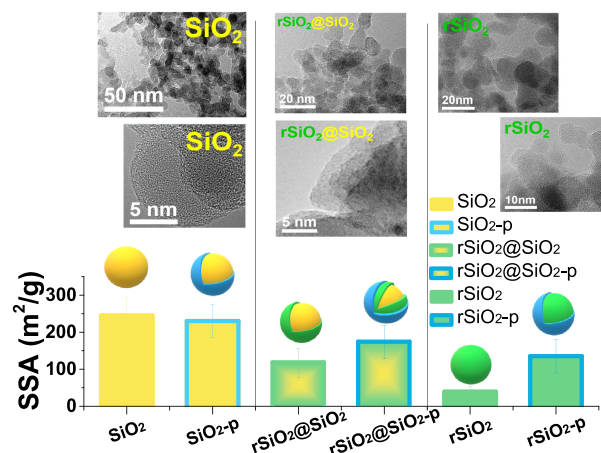nanomaterials are depicted in the top row of Figure 3. The hot- 314

Figure 3. (Upper row) TEM images of the as-prepared SiO_2, $rSiO_2@$ SiO_2, and $rSiO_2$ nanoparticles. (Lower row) Specific surface areas (m^2/g) of SiO_2, $rSiO_2@SiO_2$, and $rSiO_2$ and their passivated counterparts SiO_2-p, $rSiO_2@SiO_2$-p, and $rSiO_2$-p.

flame SiO_2 particles (Figure 3, upper left) are quasi-spherical 315
and form chain-like agglomerates, typical of FSP-made SiO_2.[5] 316
The specific surface area (Figure 3, lower row) is 260 m^2/g, 317
agreeing with spherical particles seen on the TEM images. The 318
N_2 adsorption/desorption isotherm plots are presented in 319
Figure S2, and the pore analysis is shown in Figure S3 in the 320
Supporting Information. 321
     The $rSiO_2$ particles (Figure 3, upper right) show diffused 322
structures forming soft agglomerates. Their SSA is 39 m^2/g, 323
almost six times lower than the SSA of SiO_2 particles. Thus, 324
according to the present SSA and TEM data, the formation of 325
$rSiO_2$ at lower temperatures results in soft agglomerates of 326
more diffused SiO_2 formations. The hybrid $rSiO_2@SiO_2$ 327
particles have an SSA of 117 m^2/g, intermediate to SiO_2 and 328
$rSiO_2$. According to TEM, see Figure 3, the $rSiO_2@SiO_2$ 329
particles have a core−shell-type structure with a compact/ 330
spherical SiO_2 core and a more distorted, less compacted 331
$rSiO_2$-type shell. 332
     The post-FSP treatment exerts a significant influence on the 333
SSA of the particles, see Figure 3. After FSP liquid treatment, 334
the SiO_2-p particles have an SSA of 209 m^2/g, lower than the 335
SSA of 260 m^2/g of SiO_2. TEM data (not shown) and pore 336
size analysis (Figure S3 in the Supporting Information) show 337
that after the liquid treatment, the particles have a more 338
diffused/less porous structure resembling that of the as- 339
prepared $rSiO_2$. The post-FSP treatment of $rSiO_2@SiO_2$-p 340
induces an increase of its SSA = 173 m^2/g vs the as-prepared 341
$rSiO_2@SiO_2$, see Figure 3. The SSA of $rSiO_2$-p was 342
significantly increased to 135 m^2/g, i.e., about 3 times vs the 343
as-prepared $rSiO_2$, see Figure 3. The pore size distribution data 344
(Figure S3 in the Supporting Information) indicate that the 345
post-FSP treatment in all cases induces shrinkage of the pore 346
size, attributed to condensation of silanols during the liquid 347
alkaline treatment. 348
     3.2. DLS and BET Study: The Aggregation Degree. 349
The as-prepared SiO_2, $rSiO_2@SiO_2$, and $rSiO_2$ nanosilica 350
particles form aggregates, which define their hydrodynamic size 351
in solution. The hydrodynamic sizes of the aggregates have 352

been monitored by dynamic light scattering (DLS) in aqueous suspensions at different pH values. The DLS data, see Figure 4,
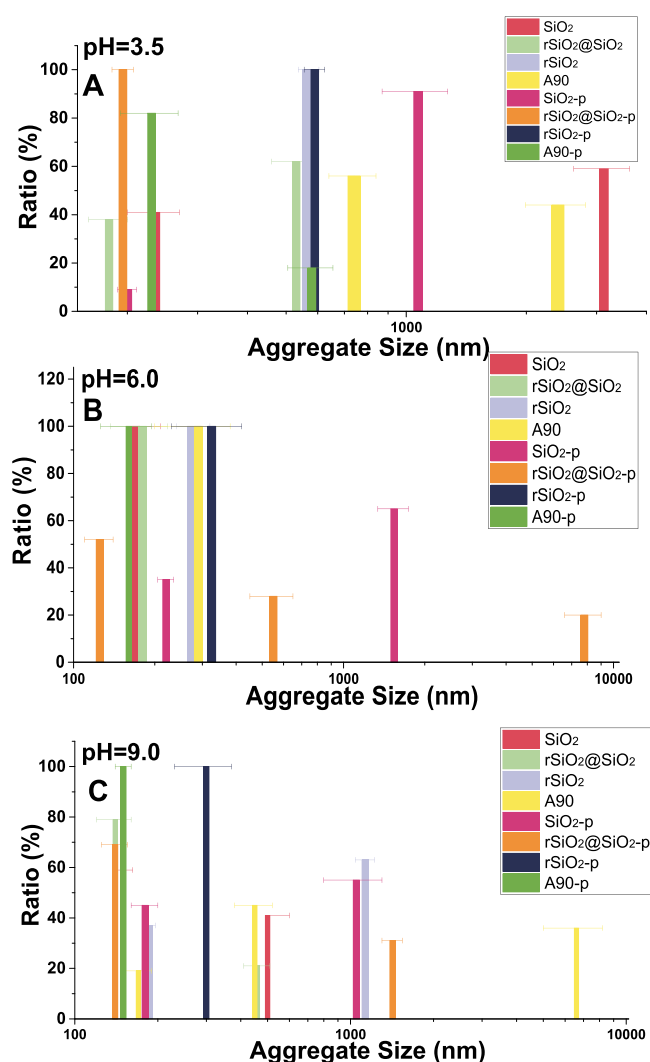
Figure 4. Aggregate size, measured with dynamic light scattering, of the nanosilica materials of the as-prepared and passivated nanosilica materials (A) in acidic pH, (B) in neutral pH, and (C) in alkaline pH.

indicate that the as-prepared high-temperature SiO_2 forms two classes of aggregates in acidic pH (Figure 4A), with mean sizes of 235 (41%) and 3130 nm (59%). At neutral pH = 6.0 (Figure 4B), SiO_2 exists in only one aggregation state with a size of 170 nm (100%), whereas at alkaline pH (Figure 4C), SiO_2 again forms two aggregation states, namely, 140 (59%) and 500 nm (41%). The hybrid $rSiO_2@SiO_2$ at acidic pH (Figure 4A) forms two families of aggregates with mean sizes of 180 (38%) and 530 nm (62%). At neutral pH (Figure 4B), only one aggregate state of 180 nm (pH = 6.0) exists. At alkaline pH (Figure 4C), $rSiO_2@SiO_2$ forms two different aggregates, namely, 140 (79%) and 460 nm (21%). Lastly, $rSiO_2$ exists in two aggregation states only at alkaline pH (Figure 4C) with 186 (37%) and 1130 nm (63%). At acidic and neutral pH, $rSiO_2$ forms monodisperse aggregates with sizes of 570 (pH = 3.5) and 280 nm (pH = 6.0). For comparison, the commercial Aerosil A90 forms two aggregate sizes in acidic pH (Figure 4A), 740 and 2400 nm, at 56 and 44%, respectively. At neutral pH (Figure 4B), A90 forms a

single aggregate with a size of 290 nm. Finally, in alkaline pH (Figure 4C), A90 forms three different aggregation states, 170 (18%), 450 (45%), and 6600 nm (36%). We notice that all our FSP nanosilica materials and the commercial A90 nanosilica create monodisperse aggregates at nearly neutral pH = 6.0.

The alkaline post-FSP treatment exerts relatively moderate changes in the aggregate size. Specifically, SiO_2-p forms one primary aggregate in acidic pH (Figure 4A), with a mean size of 1070 nm (91%) and a minor fraction (9%) of 200 nm. At neutral pH = 6 (Figure 4B), SiO_2-p forms two aggregation states, namely, 220 (35%) and 1540 nm (65%), whereas in alkaline pH (Figure 4C), the two aggregate sizes change to 180 (45%) and 1050 nm (55%).

Considering all the agglomeration dynamics data vs pH, we conclude that [i] the dominant aggregate size of high-temperature SiO_2 and SiO_2-p is near 190 ± 50 nm, and [ii] regarding the passivated hybrid $rSiO_2@SiO_2$-p, it forms one aggregate with a size of 195 ± 15 nm at acidic pH, three aggregates with sizes of 125 ± 15 (52%), 550 ± 100 (28%), and 7800 ± 1200 nm (20%) in neutral pH, and two aggregates with sizes of 140 ± 15 (69%) and 1420 ± 120 nm (31%) in alkaline pH. Again, we notice that $rSiO_2@SiO_2$ and rSiO2@SiO2-p form a stable aggregate with a mean size of 160 ± 50 nm, and [iii] the low-temperature nanosilica materials, $rSiO_2$, and $rSiO_2$-p form stable monodisperse aggregates in all three pH values, namely, 590 ± 35 (pH = 3.5), 325 ± 95 (pH = 6), and 300 ± 70 nm (pH = 9). Table S1 in the Supporting Information lists the complete data on aggregate size distribution.

3.3. Vibrational Spectroscopy. Raman spectroscopy is a well-established tool in defining the siloxane matrix since the different siloxane rings exhibit distinct vibrations. Figure 5
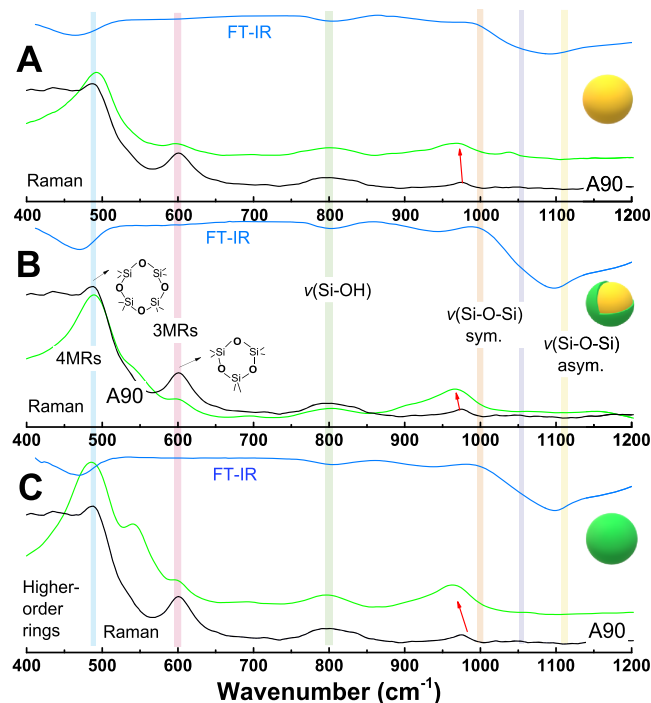
Figure 5. FT-IR and Raman spectra of the SiO_2 nanomaterials vs the A90 material. (A) SiO_2 Raman (green), IR (blue), and A90 Raman (black) spectra, (B) $rSiO_2@SiO_2$ Raman (green), IR (blue), and A90 Raman (black) spectra, and (C) $rSiO_2$ Raman (green), IR (blue), and A90 Raman (black) spectra.

presents the FT-IR and Raman spectra of the as-prepared nanosilica materials.[5] The FT-IR and Raman spectra of the FSP-made nanosilica materials show characteristic bands attributed to various structural components of the present materials: the vibrations of the siloxane matrix and the vibrations of the surface silanol groups.[10] Characteristic peaks assigned to different vibrations in Raman and FT-IR spectroscopy are listed in Table 1.

**Table 1. Characteristic Raman and FT-IR Peaks and Their Assignment**

IR (cm^{-1})	Raman (cm^{-1})	assigned peaks	ref.
~1090	~1090	$\nu(Si-O-(Si))$ asym. nonbridging O atoms	42, 43
~950	~974	isolated $\nu(Si-O(\mathbf{H}))$	5, 42, 44
~800	~800	$\nu(Si-O-(Si))$ sym.	5, 42
~600 broad	~604	3MR $\delta(Si-O-Si)$ breathing modes	5
494−423	~494	$\delta(Si-O-Si)$ asym. 4MR, 5MR, and 6MR breathing modes	5, 43

3.3.1. FT-IR Spectroscopy. All nanosilica materials display FT-IR bands assigned to the vibrations of the SiO_2 matrix and oxygen surface groups: the bands at ~1090, ~800, and ~490 cm^{-1} are due to the $Si-O-Si$ bond vibrations, and the band at ~945 cm^{-1} is due to the $Si-OH$ stretching vibration.[40] The O−H stretching motions appear as a broad peak around ~3430 cm^{-1} (Figure S4 in the Supporting Information).[41] The peaks assigned to, purportedly toxic,[4] isolated silanol groups (~3750 cm^{-1}) are negligible.[4] Fumed nanosilica exhibits additional peaks assigned to trace amounts of carbon residues formed during combustion, namely, ~2918 and ~2948 cm^{-1}

for $\nu(C-H)$ and ~1627 cm^{-1} for $\delta(O-H)$ (Figure S4 in the Supporting Information).[10] The decrease in $\nu(C-H)$ peak intensity in $rSiO_2@SiO_2$ and $rSiO_2$ compared to SiO_2 proves the success of the ring passivation method, also evident in the coated nanomaterial (Figure S4 in the Supporting Information). Lastly, control FT-IR data of the precursor HMDSO (Figure S5 in the Supporting Information) confirms the assignment of the peak at ~1270 cm^{-1} to the $Si-CH_3$ moieties from HMDSO. Table 1 provides a list of assignments of the characteristic peaks of nanosilica.

3.3.2. Raman Spectroscopy. Typically, the Raman spectrum of SiO_2 materials is characterized by features in the region of 400−600 cm^{-1}, see Figure 5, which correspond to different configurations of the siloxane rings.[5] In our materials, differences in the Raman spectra are noticed upon passivation by alkaline treatment (see Figure 5 and Figure S6 in the Supporting Information). New peaks appear (below ~400 cm^{-1}), which are assigned to bigger-than-four-membered siloxane rings in the matrix after the alkaline pH-induced condensation, namely, toward 5MRs and 6MRs.[5] The noticeable difference between as-prepared SiO_2 and SiO_2-p indicates that the liquid treatment modified the siloxane framework toward larger rings. In this aspect, the formation of larger siloxane rings indicates a less strained network toward more "relaxed" configurations. In the same context, larger, more "relaxed" siloxane rings are formed in the hybrid $rSiO_2@SiO_2$ and the low-T $rSiO_2$ during the alkaline passivation.

Additionally, multiple downshifts of peaks are noticed in Figure 5, indicative of less strained lattices. The red arrow in Figure 5 indicates that the bump at ~974 cm^{-1} in the commercial A90 shifted to ~965 cm^{-1} in the low-T $rSiO_2$, the same for the ~837 cm^{-1} peak, which shifted to ~797 cm^{-1}, and the 600 cm^{-1} peak downshifted to ~542 cm^{-1}. The band at ~547 cm^{-1} in the Raman spectra can be attributed to a $Si-$
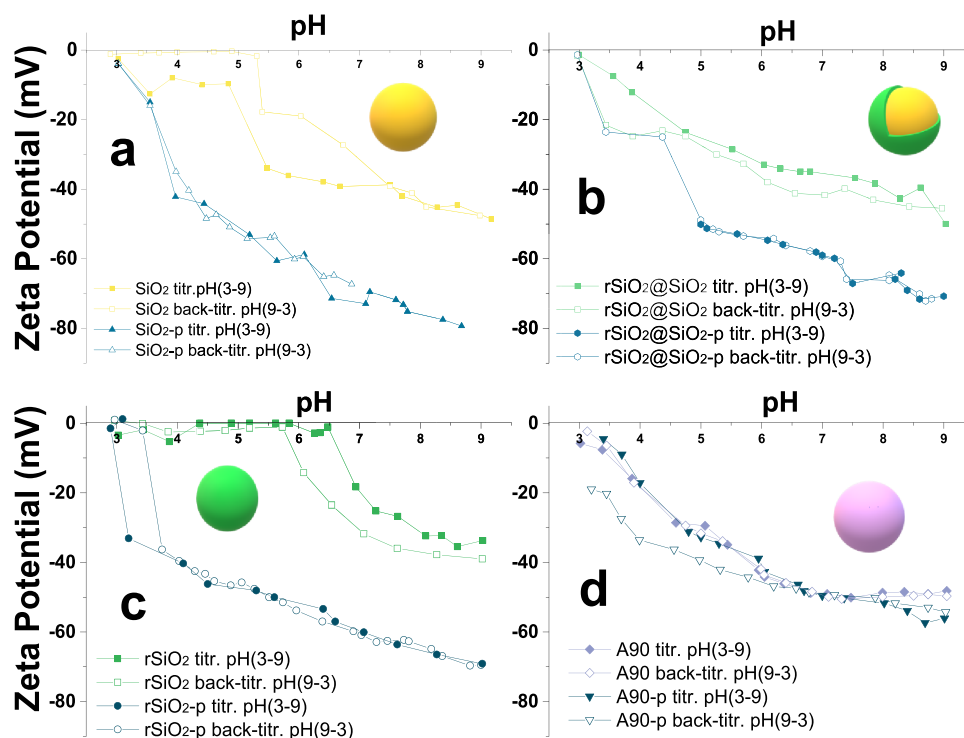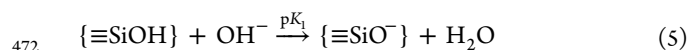

Figure 6. Zeta potential (mV) of (a) SiO_2 and SiO_2-p, (b) $rSiO_2@SiO_2$ and $rSiO_2@SiO_2$-p, (c) $rSiO_2$ and $rSiO_2$-p, and (d) A90 and A90-p nanosilica materials.
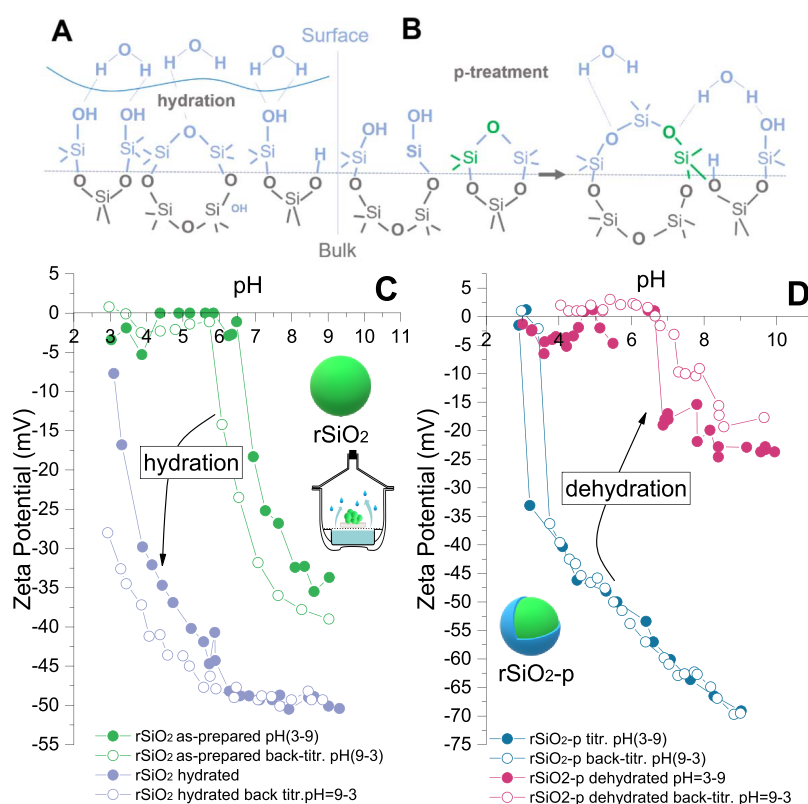
Figure 7. (A) Water adsorption during hydration of the nanosilica powder, placed in a desiccator with water under a vacuum, (B) deprotonation, ring opening, condensation, and water adsorption during the alkaline post-FSP treatment, (C) zeta potential (mV) of the as-prepared and hydrated rSiO$_2$ for 48 h, and (D) zeta potential (mV) of the as-prepared and dehydrated rSiO$_2$-p for 24 h.

CH$_3$ moiety from HMDSO. This is observed only in the low-T rSiO$_2$, rSiO$_2$@SiO$_2$, and their passivated counterparts. It is absent in the high-T SiO$_2$ and A90. This indicates that the lower-temperature process in rSiO$_2$ and rSiO$_2$@SiO$_2$ allows some Si−CH$_3$ moieties from HMDSO to be present in low-T rSiO$_2$ and rSiO$_2$@SiO$_2$, and these moieties are not altered by the liquid treatment.

3.4. SiO$_2$ Surface Charge: A Zeta Potential Study. In nanosilica materials, the types of silanols on the surface determine the pK_a values of the surface reactions.[45] In a water dispersion, the surface silanols (≡Si−OH) determine surface charge of the nanomaterials *via* the protonation/deprotonation reactions 5 and 6.[40,46]

$$\{\equiv SiOH\} + OH^- \xrightarrow{pK_1} \{\equiv SiO^-\} + H_2O \qquad (5)$$

$$\{\equiv Si-OH_2^+\} \xrightarrow{pK_2} \{\equiv SiOH\} + H^+ \qquad (6)$$

The symbol {≡} signifies that the species are formed on the surface of the silica particles *via* interactions with the liquid phase, H$^+$ and OH$^-$. In this context, the concentration of H$^+$ and OH$^-$ is determined by pH. The equilibrium in reactions 5 and 6 is dictated by the pK_1 and pK_2 values, determining the surface protonation/deprotonation mechanisms.[40] Typically, the pK_2 value is ∼2.0.[46] Therefore, the SiO$_2$ surface is nonprotonated at pH > 2.0, i.e., reaction 6 makes a minor contribution at the typical pH range of 3.0−9.0. On the other hand, the pK_1 value is typically 6.0−7.0. Reaction 5 therefore prevails at all physiological pH values. In this context, it is well-anticipated that silica would be either noncharged at pK_2 < pH < pK_1 or negatively charged at pH > pK_2.

Different titration protocols have been followed to study how consecutive alterations of pH affect the dissociation of the surface groups. Figure 6 presents the zeta potential profile *vs* pH of our three types of nanosilica particles. When increasing the pH from acidic to alkaline values, the isoelectric point (IEP) of the as-prepared SiO$_2$ and rSiO$_2$@SiO$_2$ NPs was pH$_{IEP}$ = 3.0. In comparison, the commercial A90 nanosilica had a pH$_{IEP}$ of ∼3.0. These values (IEP ∼ pH = 2.0−3.0) are typical of flame-engineered nanosilica materials.[46] After reaching the pH = 9.0 value, the particles were incubated for 15 min and back-titrated toward acidic pH. In this titration process, the IEP of the as-prepared SiO$_2$ shifted from pH$_{IEP}$ = 3.0 to pH$_{IEP}$ = 4.8 (Figure 6, panel a), with a concurrent decrease in the zeta potential values (less negative). Subsequent acid-to-alkaline pH titrations show no further changes in the IEP or zeta potential (data not shown). As described by reaction 5, ≡Si−OH groups get deprotonated to form ≡Si−O$^-$ groups during the pH increase toward alkaline values, while they get reprotonated in the back-titration. In this context, after exposure to alkaline pH, the pK_a of the ≡Si−OH groups increases, namely, the pH$_{IEP}$ = 3.0 increases to pH$_{IEP}$ = 4.8.

After a short alkaline incubation, it is probably more difficult for the deprotonation of the surface ≡Si−OH groups to occur, i.e., the association of surface ≡Si−O$^-$ units with the interfacial H$^+$ becomes stronger. This phenomenon was observed for all our FSP-made particles. The pH titration data of rSiO$_2$@SiO$_2$ (Figure 6, panel b) reveals that the surface charge distribution is slightly altered when the pH decreases from alkaline to acidic, evidenced by the more negative zeta potential. However, the pH$_{IEP}$ value of rSiO$_2$@SiO$_2$ did not change. The zeta potential of rSiO$_2$ increases slightly (more

negative values) in pH values greater than the pH_{IEP}. The pH_{IEP} remained unchanged at a value of 5.8.

Overall, the present surface charge results can be summarized as follows: [i] the as-prepared $rSiO_2$ material has a $\equiv Si-OH$ pK_a value of 5.8, which is not changed upon exposure to alkaline pH, and [ii] the as-prepared SiO_2 material has $\equiv Si-OH$ with a more acidic pKa value (2.3), which is strongly upshifted upon exposure to alkaline pH. An explanation for this could be the presence of different groups on the surface that have been created during the FSP synthesis. The ring-sprayed silica facilitates the formation of less pH-dependent $\equiv Si-O-Si \equiv$ siloxane bridges that coexist on the surface with silanols. The presence of mainly $\equiv Si-O-Si \equiv$ moieties on the surface of $rSiO_2$ can additionally explain the minor alteration in the line shapes of the consecutive pH titrations compared to SiO_2. Moreover, the lower FSP temperature could facilitate the presence of protonated silanols ($\equiv Si-OH$), whereas the high-temperature nanosilica seems to generate mainly $Si-O^-$ moieties. The zeta potential analysis provides vital information about the hydroxyl groups on the surface in terms of affinity and pK_a. Based on the results, it is clear that the strained, high-temperature SiO_2 has a more hydroxylated surface than the passivated/low-temperature nanosilica, where (a) the siloxane structures prevail and (b) the presence of aliphatic carbon traces possibly alter the pK_a of the surface groups toward more alkaline values.

Since the short exposure of the particles to alkaline pH, i.e., during the pH titration, was able to induce alterations on the surface groups of the FSP silica, our hypothesis was that a more elaborated liquid passivation, i.e., the "p"-labeled materials, is expected to impact the siloxane ring opening and consequently the condensation of silanol groups to siloxanes. As depicted in Figure 6, [i] the changes in the successive acid–base titrations of all p-nanosilica materials were insignificant since the acid-to-alkaline or the back-titration curves are practically identical, and [ii] the formed outer shell of p-nanosilica materials leads to a consistency between the pH_{IEP} values, which is $pH_{IEP} = 3.0$ in all cases. As supported by the Raman analysis, the p-treatment promotes the formation of bigger $\equiv Si-O-Si \equiv$ siloxane bridges of the FSP silica materials.[47,48] Moreover, as shown in the titration curves in Figure 6, the zeta potential reaches significantly more negative values, i.e., compared to the as-prepared nanomaterials, indicating that the p-layer may also interact with water molecules.

After the liquid passivation, H_2O molecules are expected to be adsorbed in the amorphous nanosilica surface, as shown in Figure 7b; these weak hydrogen-bond interactions can form a surface–water interface that could contribute to the pH_{IEP} and the total surface charge. This way, particles show a unified and stable $pH_{IEP} = 3.0$ and become more negatively charged than their homologous as-prepared materials.

The commercial flame nanosilica A90 remained inert as we observed no significant changes in the two consecutive titrations. The exposure to alkaline pH or liquid passivation had no impact on the surface charge of A90. An explanation for this could be the formation of stable, hydrated structures on the surface of A90 due to the aging of the particular nanosilica batch since it was not a freshly prepared nanomaterial (shelf time > 1 year). However, more research is needed for this evaluation.

3.4.1. Effect of Water Adsorption.
A series of experiments, including hydration/dehydration, have been additionally carried out to investigate further the effect of water adsorption/desorption on the surface charge. As depicted in Figure 7, hydration of the as-prepared $rSiO_2$ after exposure to a H_2O-saturated atmosphere leads to water physisorption and a $pH_{IEP} = 3.0$. In this aspect, after mildly heating (40 °C) $rSiO_2$-p under a vacuum for 24 h, the IEP of dehydrated $rSiO_2$-p shifted from $pH_{IEP} = 3.0$ to $pH_{IEP} = 6.7$. Apparently, under mild heating (40 °C) under a vacuum, physisorbed H_2O molecules were removed. To summarize, the IEP of the of-industrial-interest (as-prepared) nanosilica materials seemed to [i] increase by design (during the FSP-ring passivation) and [ii] be altered under liquid alkaline and/or hydration treatment.

3.5. Reactive Oxygen Species Generation.
Electron paramagnetic resonance (EPR) spectroscopy detects free hydroxyl radicals that lead to oxidative stress and cell damage. A spin-trap molecule is needed to monitor hydroxyl radical generation in our systems. Here, we use 5,5-dimethyl-1-pyrroline *N*-oxide (DMPO) as a spin trap and 2,2-diphenyl-1-picrylhydrazyl (DPPH) as a spin standard.[21,29]

The typical signal of the DMPO-OH adduct is presented in Figure 8.[21] The as-prepared SiO_2, $rSiO_2@SiO_2$, and $rSiO_2$
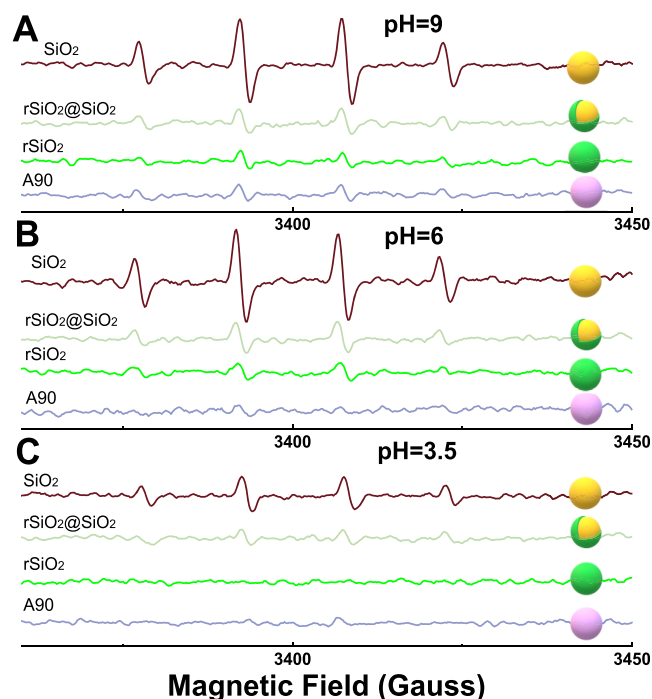
Figure 8. EPR signals (typical of the DMPO-OH adduct) of the ROS produced by FSP-made nanosilica materials in (A) pH = 9.0, (B) pH = 6.0, and (C) pH = 3.5.

generate $^\bullet OH$ radicals in the presence of H_2O_2. No radicals were detected in the absence of the nanoparticles. Thus, the generation of $^\bullet OH$ radicals is a surface-initiated phenomenon. The first observation is that the high-*T* strained SiO_2 nanosilica produces more hydroxyl radicals than $rSiO_2@SiO_2$ and $rSiO_2$. The hybrid $rSiO_2@SiO_2$ $^\bullet OH$ radical generation was between the generation capacity of $rSiO_2$ and SiO_2. The ring-made $rSiO_2$ nanosilica, on the opposite, produces a lower, almost insignificant, amount of $^\bullet OH$ radicals. A second observation is that the general trend of radical generation, which follows the order $SiO_2 > rSiO_2@SiO_2 > rSiO_2$, was not affected by the pH
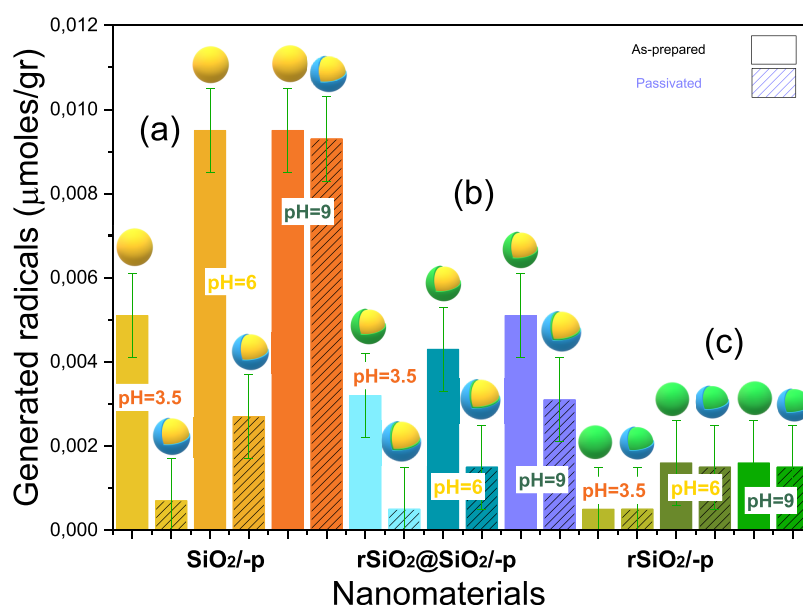
Figure 9. Hydroxyl radical ($^{\bullet}$OH) yields per gram of the as-prepared materials (nonhatched bars) and their passivated counterparts (hatched bars) at different pH values. Group (a) refers to SiO_2 (nonhatched bar) and SiO_2-p (hatched bar), group (b) to hybrid $rSiO_2@SiO_2$ (nonhatched bar) and $rSiO_2@SiO_2$-p (nonhatched bar), and group (c) to $rSiO_2$ (nonhatched bar) and $rSiO_2$-p (hatched bar).

alteration but could probably match the surface area decrease (Figure 3). This way, the small specific surface area of $rSiO_2$ results in a reduced interaction with H_2O_2 and thus lowers ROS production.

Acidic pH seems to decrease the ROS generation capacity in all materials. An increase in the pH facilitates the homolytic cleavage of H_2O_2 and, therefore, the $^{\bullet}$OH generation ability.[23] Our results confirm that the hydroxyl radicals' generation increased in all cases at neutral and alkaline pH in the as-prepared nanosilica materials as well as in their post-FSP passivated counterparts. More specifically, at acidic pH, the radical generation capacity of the as-prepared composite $rSiO_2@SiO_2$ was lower, i.e., by 37.0%, whereas the decrease was more prominent in $rSiO_2$ (79.0% lower ROS generation). Accordingly, the radical generation capacity was reduced at neutral pH values by 54.7% in $rSiO_2@SiO_2$ and by 83.2% in the passivated $rSiO_2$. Finally, the observed decreases were 46.3 and 83.2% at alkaline pH for $rSiO_2@SiO_2$ and $rSiO_2$, respectively.

The high-T strained SiO_2 nanosilica produced the same amount of hydroxyl radicals at neutral and alkaline pH and fewer at acidic pH (as depicted in Figure 9). After liquid passivation, the hydroxyl radical generation capacity of SiO_2 decreased significantly at acidic (80.4%) and neutral pH (71.6%) but remained practically the same in alkaline pH (2.1% decrease). As mentioned above, more ROS were generated by the as-prepared hybrid $rSiO_2@SiO_2$, while they were significantly decreased after the liquid treatment at all pH values. In fact, after the alkaline liquid treatment, the hydroxyl radical generation capacity of $rSiO_2@SiO_2$ decreased by the same degree at acidic (65.6%) and neutral pH (65.1%) and less in alkaline pH (39.3% decrease). Lastly, the low-T $rSiO_2$ generated the same amount of hydroxyl radicals in neutral and alkaline pH and less in acidic pH. Moreover, we notice no significant change in the ROS generation after the liquid passivation; this is attributed to the increase in the SSA from 39 ± 15 m^2/g for $rSiO_2$ to 135 ± 45 m^2/g for $rSiO_2$-p, which probably counterbalances the positive effect of passivation.

This fact states that the low-T FSP synthesis of $rSiO_2$ results in a passivated configuration, namely, a fumed nanosilica with low ROS generation, which does not need further liquid passivation. In general, liquid passivation induced no significant decrease in the radical generation capacity of $rSiO_2$, i.e., by ~6.2% at pH = 6.0 and pH = 9.0.

As a control, the as-received reference commercial A90 generally produced the same $^{\bullet}$OH radicals as the low-T $rSiO_2$ (see Table S2 in the Supporting Information). We considered that this commercial material had been exposed to ambient humidity for an extended period; therefore, its surface had been modified. We have treated A90 at 350 °C for $t = 300$ min to test this hypothesis. This resulted in a significant increase in the ROS generation capacity (data not shown).

Based on the present EPR and Raman data, we conclude that [i] the high-temperature SiO_2 consists of a predominantly strained siloxane matrix and produces more $^{\bullet}$OH radicals. [ii] Coating high-temperature SiO_2 with a low-temperature $rSiO_2$, which bears a more "relaxed" inert siloxane matrix, results in a hybrid $rSiO_2@SiO_2$ nanomaterial with a lower $^{\bullet}$OH radical generation capacity. [iii] In low-temperature $rSiO_2$, the $^{\bullet}$OH radical production is insignificant. The elimination of $^{\bullet}$OH radical production in $rSiO_2$ happens because larger, less strained siloxane rings prevail, which is a crucial finding of the present study. Hereafter, the findings on the ROS generation are correlated with the acute toxicity of the FSP nanosilica materials.

3.6. Acute Toxicity and Microtox Evaluation. To strengthen our overall understanding of the physicochemical profile of the engineered nanosilica materials, we carried out a series of acute toxicity tests. We used a Microtox LX analyzer by Modern Water to assess the acute toxicity through bioluminescence quantification of the nonpathogenic, marine bacterial strain *Allivibrio fischeri* (*Vibrio fischeri*). The acute toxicity is calculated after short-term exposure, in this work after 15 min, to study potential toxic effects that appear immediately after direct exposure. The data in Figure 10 show that the effective concentration (EC_{50}) that induces a 50%
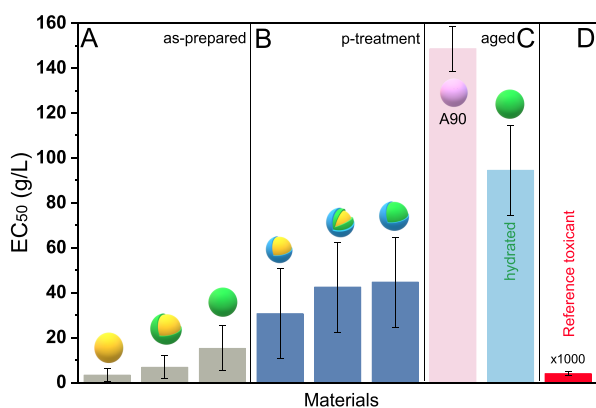
Figure 10. Effective concentration (EC_{50}) of (A) as-prepared SiO_2, $rSiO_2@SiO_2$, and $rSiO_2$, (B) post-synthetically passivated SiO_2-p, $rSiO_2@SiO_2$-p, and rSiO2-p, (C) commercial A90 and hydrated as-prepared $rSiO_2$ nanosilica materials, and (D) reference toxicant zinc sulfate (value multiplied by 1000).

decrease in the luminescence intensity was 3.3 (as-prepared SiO_2), 6.8 (as-prepared $rSiO_2@SiO_2$), and 15.2 g/L (as-prepared $rSiO_2$). Thus, we conclude that the low-T $rSiO_2$ has a significantly lower acute toxicity potential than high-T SiO_2. The post-FSP-treated materials showed a dramatic decrease in acute toxicity toward *Allivibrio fischeri*, i.e., 30.7 (SiO_2-p), 42.5 ($rSiO_2@SiO_2$-p), and 44.7 g/L ($rSiO_2$-p). The EC_{50} values indicate that the as-prepared high-T SiO_2 induces a considerably more significant acute toxic effect on the bacteria than the post-synthetically passivated SiO_2-p. The reference zinc sulfate toxicant gave an EC_{50} of 4.26 mg/L (~0.004 g/L), i.e., due to Zn^{2+} ions.[16]

Interestingly, the EC_{50} value of A90 reached 148.63 g/L. As mentioned above, we assume that stable, hydrated structures form on the surface of A90 due to long shelf-time. Thus, to confirm our hypothesis, we measured the acute toxicity of hydrated $rSiO_2$ (as described in Section 3.4) that gave an EC_{50} of 94.5 g/L, which is less toxic than its liquid passivated counterpart ($rSiO_2$-p). We conclude that long-term exposure to ambient humidity can lead to more passivated, less toxic silica structures.

4. DISCUSSION

So far, it is anticipated that multiple factors can modulate the toxicity of engineered nanoparticles; however, ROS generation holds a critical position among them, especially in the case of nanosilica.[49] Zhang *et al.* correlated the ROS-induced toxicity of nanosilica to the strain of the siloxane rings.[5] Our findings confirm that the presence of larger, less strained, siloxane rings leads to a decrease in ROS generation and acute toxicity. The present data also corroborate the work of Spyrogianni *et al.*[28] as we directly connect the FSP flame temperature to the silica matrix formation and the surface characteristics[28] and prove a direct correlation with ROS generation capacity and acute toxicity of nanosilica. Furthermore, our Raman data show that in low-T $rSiO_2$, the siloxane rings are more easily converted to bigger/less strained siloxane rings, i.e., 4MRs, 5MRs, and 6MRs, while in the high-T SiO_2, the strained 3MRs prevail. Technology-wise, the low-temperature FSP process for the production of $rSiO_2$ leads to a nanosilica matrix consisting of less strained siloxane rings (depicted in Figure S6 in the Supporting Information). The ROS generation capacity decrease is analogous to the [i] increase in siloxane ring size

and [ii] the SSA decrease, whereas the siloxane ring formation seems to be the dominant beneficial mechanism. According to the present DLS data, the aggregate sizes of our FSP nanosilica materials appear to be in the same size range at neutral pH values. Considering this, the characteristic toxicity differences detected in the present Microtox analysis indicate that aggregate sizes do not seem to be the major factor in the toxicity profile of the FSP nanosilica materials. Acute toxicity is correlated with ROS generation, as shown by EPR. Given the industrial-scale character of our FSP protocols, in future studies, it would be helpful to further evaluate the toxicity of FSP silica nanostructures on mammalian and/or other types of cells in order to eliminate chronic toxic effects.[50]

5. CONCLUSIONS

Herein, we exemplify two possible strategies for the production of more passivated/less toxic nanosilica: a one-step, low-temperature FSP process and a two-step process that includes a post-FSP liquid treatment protocol. Structurally, both lead to the same result, which is forming larger siloxane rings, which in turn lead to a decrease in ROS generation and acute toxicity. Among the silica materials engineered herein, the low-T $rSiO_2$ can be considered as an optimal material, i.e., either as-prepared by FSP or even better after a simple hydration step. Technology-wise, using the FSP technology, we can engineer nanosilica materials in one step, safer-by-design, i.e., we can skip post-synthetic liquid treatments by utilizing a simple-to-adopt low-T FSP configuration. Thus, the present study demonstrates a cost-effective approach, specifically appropriate for producing low-toxicity nanosilica at an industrial scale.

■ ASSOCIATED CONTENT

ⓢ Supporting Information

The Supporting Information is available free of charge at https://pubs.acs.org/doi/10.1021/acsanm.2c01273.

(Figure S1) Calibration curve of DLS size measurement; (Figure S2) N_2 adsorption−desorption isotherms of SiO_2, $rSiO_2@SiO_2$, $rSiO_2$, SiO_2-p, $rSiO_2@SiO_2$-p, and $rSiO_2$-p; (Figure S3) pore analysis of the as-prepared and post-treated nanosilica materials; (Figure S4) FT-IR spectra of the nanosilica materials in the range of 4000−400 cm^{-1}; (Figure S5) FT-IR spectra of the precursor HMDSO in the range of 4000−400 cm^{-1}; (Figure S6) deconvolution of the Raman spectral characteristic bands of SiO_2, SiO_2-p, $rSiO_2@SiO_2$, $rSiO_2@SiO_2$-p, $rSiO_2$, and $rSiO_2$-p nanosilica materials that are attributed to the vibrations of the siloxane matrix; (Figure S7) Raman analysis of commercially available nanosilica A90; (Table S1) aggregation size of the engineered nanosilica structures at different pH values; (Table S2) μmol/g of hydroxyl radicals generated from the nanosilica materials (PDF)

■ AUTHOR INFORMATION

Corresponding Authors

Yiannis Deligiannakis − *Laboratory of Physical Chemistry of Materials & Environment, Department of Physics, University of Ioannina, GR-45110 Ioannina, Greece;* ⓞ orcid.org/0000-0002-9390-4222; Phone: +302651008662; Email: ideligia@uoi.gr

Maria Louloudi − *Laboratory of Biomimetic Catalysis & Hybrid Materials, Department of Chemistry, University of*

Ioannina, GR-45110 Ioannina, Greece;

Phone: +302651008418; Email: mlouloud@uoi.gr

Authors

Fotini Fragou − *Laboratory of Biomimetic Catalysis & Hybrid Materials, Department of Chemistry, University of Ioannina, GR-45110 Ioannina, Greece;* ⓘ orcid.org/0000-0001-5302-3159

Panagiota Stathi − *Laboratory of Physical Chemistry of Materials & Environment, Department of Physics, University of Ioannina, GR-45110 Ioannina, Greece;* ⓘ orcid.org/0000-0002-5936-3354

Complete contact information is available at:
https://pubs.acs.org/10.1021/acsanm.2c01273

Notes

The authors declare no competing financial interest.

■ REFERENCES

(1) Yan, L.; Zhao, F.; Wang, J.; Zu, Y.; Gu, Z.; Zhao, Y. A Safe-by-Design Strategy towards Safer Nanomaterials in Nanomedicines. *Adv. Mater.* **2019**, *31*, 1805391.

(2) Croissant, J. G.; Butler, K. S.; Zink, J. I.; Brinker, C. J. Synthetic Amorphous Silica Nanoparticles: Toxicity, Biomedical and Environmental Implications. *Nat. Rev. Mater.* **2020**, *5*, 886−909.

(3) Pavan, C.; Delle Piane, M.; Gullo, M.; Filippi, F.; Fubini, B.; Hoet, P.; Horwell, C. J.; Huaux, F.; Lison, D.; Lo Giudice, C.; Martra, G.; Montfort, E.; Schins, R.; Sulpizi, M.; Wegner, K.; Wyart-Remy, M.; Ziemann, C.; Turci, F. The Puzzling Issue of Silica Toxicity: Are Silanols Bridging the Gaps between Surface States and Pathogenicity? *Part. Fibre Toxicol.* **2019**, *16*, 1−10.

(4) Pavan, C.; Santalucia, R.; Leinardi, R.; Fabbiani, M.; Yakoub, Y.; Uwambayinema, F.; Ugliengo, P.; Tomatis, M.; Martra, G.; Turci, F.; Lison, D.; Fubini, B. Nearly Free Surface Silanols Are the Critical Molecular Moieties That Initiate the Toxicity of Silica Particles. *Proc. Natl. Acad. Sci. U. S. A.* **2020**, *117*, 27836−27846.

(5) Zhang, H.; Dunphy, D. R.; Jiang, X.; Meng, H.; Sun, B.; Tarn, D.; Xue, M.; Wang, X.; Lin, S.; Ji, Z.; Li, R.; Garcia, F. L.; Yang, J.; Kirk, M. L.; Xia, T.; Zink, J. I.; Nel, A.; Brinker, C. J. Processing Pathway Dependence of Amorphous Silica Nanoparticle Toxicity: Colloidal vs Pyrolytic. *J. Am. Chem. Soc.* **2012**, *134*, 15790−15804.

(6) Madler, L.; Kammler, H. K.; Mueller, R.; Pratsinis, S. E. Controlled Synthesis of Nanostructured Particles by Ame Spray Pyrolysis. *J. Aerosol Sci.* **2002**, *33*, 369−389.

(7) Strobel, R.; Pratsinis, S. E. Flame Aerosol Synthesis of Smart Nanostructured Materials. *J. Mater. Chem.* **2007**, 4743−4756.

(8) Teoh, W. Y.; Amal, R.; Mädler, L. Flame Spray Pyrolysis : An Enabling Technology for Nanoparticles Design and Fabrication. *Nanoscale* **2010**, 1324−1347.

(9) Gröhn, A. J.; Pratsinis, S. E.; Sánchez-Ferrer, A.; Mezzenga, R.; Wegner, K. Scale-up of Nanoparticle Synthesis by Flame Spray Pyrolysis: The High-Temperature Particle Residence Time. *Ind. Eng. Chem. Res.* **2014**, *53*, 10734−10742.

(10) Fragou, F.; Moularas, C.; Adamska, K.; Deligiannakis, Y.; Louloudi, M. Mn(II)-Based Catalysts Supported on Nanocarbon-

(11) Moularas, C.; Georgiou, Y.; Adamska, K.; Deligiannakis, Y. Thermoplasmonic Heat Generation Efficiency by Nonmonodisperse Core−Shell Ag 0 @SiO 2 Nanoparticle Ensemble. *J. Phys. Chem. C* **2019**, *123*, 22499−22510.

(12) Pokhrel, S.; Mädler, L. Flame-Made Particles for Sensors, Catalysis, and Energy Storage Applications. *Energy Fuels* **2020**, *34*, 13209−13224.

(13) Ganguly, P.; Breen, A.; Pillai, S. C. Toxicity of Nanomaterials: Exposure, Pathways, Assessment, and Recent Advances. *ACS Biomater. Sci. Eng.* **2018**, *4*, 2237−2275.

(14) Chen, L.; Liu, J.; Zhang, Y.; Zhang, G.; Kang, Y.; Chen, A.; Feng, X.; Shao, L. The Toxicity of Silica Nanoparticles to the Immune System. *Nanomedicine* **2018**, *13*, 1939−1962.

(15) Pokhrel, S.; Nel, A. E.; Mädler, L. Custom-Designed Nanomaterial Libraries for Testing Metal Oxide Toxicity. *Acc. Chem. Res.* **2013**, *46*, 632−641.

(16) He, X.; Aker, W. G.; Fu, P. P.; Hwang, H.-M. Toxicity of Engineered Metal Oxide Nanomaterials Mediated by Nano-Bio-Eco-Interactions: A Review and Perspective. *Environ. Sci.: Nano* **2015**, 564−582.

(17) Smith, D. K. Nomenclature of the Silica Minerals and Bibliography. *Powder Diffr.* **1998**, *13*, 2−19.

(18) Brinker, C. J.; Butler, K. S.; Garofalini, S. H. Are Nearly Free Silanols a Unifying Structural Determinant of Silica Particle Toxicity? *Proc. Natl. Acad. Sci. U. S. A.* **2020**, *117*, 30006−30008.

(19) Yu, Z.; Li, Q.; Wang, J.; Yu, Y.; Wang, Y.; Zhou, Q.; Li, P. Reactive Oxygen Species-Related Nanoparticle Toxicity in the Biomedical Field. *Nanoscale Res. Lett.* **2020**, *15*, 115.

(20) Toxicol, A.; Murugadoss, S.; Lison, D.; Godderis, L.; Van Den Brule, S.; Mast, J.; Brassinne, F.; Sebaihi, N.; Hoet, P. H. Toxicology of Silica Nanoparticles : An Update. *Arch. Toxicol.* **2017**, 2967.

(21) Lehman, S. E.; Morris, A. S.; Mueller, P. S.; Salem, A. K.; Grassian, V. H.; Larsen, S. C. Silica Nanoparticle-Generated ROS as a Predictor of Cellular Toxicity: Mechanistic Insights and Safety by Design. *Environ. Sci.: Nano* **2016**, *3*, 56−66.

(22) Manke, A.; Wang, L.; Rojanasakul, Y. Mechanisms of Nanoparticle-Induced Oxidative Stress and Toxicity. *BioMed Res. Int.* **2013**, No. 942916.

(23) Nosaka, Y.; Nosaka, A. Y. Generation and Detection of Reactive Oxygen Species in Photocatalysis. *Chem. Rev.* **2017**, *117*, 11302−11336.

(24) Rubio, L.; Pyrgiotakis, G.; Beltran-Huarac, J.; Zhang, Y.; Gaurav, J.; Deloid, G.; Spyrogianni, A.; Sarosiek, K. A.; Bello, D.; Demokritou, P. Safer-by-Design Flame-Sprayed Silicon Dioxide Nanoparticles: The Role of Silanol Content on ROS Generation, Surface Activity and Cytotoxicity. *Part. Fibre Toxicol.* **2019**, *16*, 40.

(25) Lushchak, V. I. Free Radicals , Reactive Oxygen Species, Oxidative Stresses and Their Classifications Chemico-Biological Interactions Free Radicals, Reactive Oxygen Species, Oxidative Stress and Its Classification. *Chem.-Biol. Interact.* **2016**, *224*, 164−175.

(26) Nabeshi, H.; Yoshikawa, T.; Matsuyama, K.; Nakazato, Y.; Tochigi, S.; Kondoh, S.; Hirai, T.; Akase, T.; Nagano, K.; Abe, Y.; Yoshioka, Y.; Kamada, H.; Itoh, N.; Tsunoda, S.-i.; Tsutsumi, Y. Amorphous Nanosilica Induce Endocytosis-Dependent ROS Generation and DNA Damage in Human Keratinocytes. *Part. Fibre Toxicol.* **2011**, *8*, 1.

(27) Wang, S.; Guo, H.; Li, Y.; Li, X. Penetration of Nanoparticles across a Lipid Bilayer: Effects of Particle Stiffness and Surface Hydrophobicity. *Nanoscale* **2019**, *11*, 4044−4034.

(28) Spyrogianni, A.; Herrmann, I. K.; Keevend, K.; Pratsinis, S. E.; Wegner, K. The Silanol Content and in Vitro Cytolytic Activity of Flame-Made Silica. *J. Colloid Interface Sci.* **2017**, *507*, 95−106.

(29) Deligiannakis, Y.; Sotiriou, G. A.; Pratsinis, S. E. Antioxidant and Antiradical SiO2 Nanoparticles Covalently Functionalized with Gallic Acid. *ACS Appl. Mater. Interfaces* **2012**, *4*, 6609−6617.

(30) He, W.; Liu, Y.; Wamer, W. G.; Yin, J. J. Electron Spin Resonance Spectroscopy for the Study of Nanomaterial-Mediated

Coated Silica Nanoparticles for Alkene Epoxidation. *ACS Appl. Nano Mater.* **2020**, *6*, 5583−5592.

Generation of Reactive Oxygen Species. *J. Food Drug Anal.* **2014**, *22*, 49−63.

(31) Psathas, P.; Georgiou, Y.; Moularas, C.; Armatas, G. S.; Deligiannakis, Y. Controlled-Phase Synthesis of Bi_2Fe4O_9 & $BiFeO_3$ by Flame Spray Pyrolysis and Their Evaluation as Non-Noble Metal Catalysts for Efficient Reduction of 4-Nitrophenol. *Powder Technol.* **2020**, *368*, 268−277.

(32) Teleki, A.; Heine, M. C.; Krumeich, F.; Akhtar, M. K.; Pratsinis, S. E. In Situ Coating of Flame-Made TiO_2 Particles with Nanothin SiO_2 Films. *No.* **2008**, *1*, 12553−12558.

(33) Sotiriou, G. A.; Sannomiya, T.; Teleki, A.; Krumeich, F.; Vörös, J.; Pratsinis, S. E. Non-Toxic Dry-Coated Nanosilver for Plasmonic Biosensors. *Adv. Funct. Mater.* **2010**, *20*, 4250−4257.

(34) Jossen, R.; Pratsinis, S. E.; Stark, W. J.; Mädler, L. Criteria for Flame-Spray Synthesis of Hollow, Shell-like, or Inhomogeneous Oxides. *J. Am. Ceram. Soc.* **2005**, *88*, 1388−1393.

(35) Sotiriou, G. A.; Blattmann, C. O.; Deligiannakis, Y. Nano-antioxidant-Driven Plasmon Enhanced Proton-Coupled Electron Transfer. *Nanoscale* **2016**, *8*, 796−803.

(36) Sotiriou, G.; Gass, S.; Pratsinis, S. E. Hermetically Coated Nanosilver: No Ag^+ Ion Leaching. *Mater. Res. Soc. Symp. Proc.* **2012**, *1386*, 56−61.

(37) Teleki, A.; Akhtar, M. K.; Pratsinis, S. E. The Quality of SiO_2-Coatings on Flame-Made TiO_2-Based Nanoparticles. *J. Mater. Chem.* **2008**, *18*, 3547−3555.

(38) Yaws, C. L. *The Yaws Handbook of Vapor Pressure: Antoine Coefficients*: Gulf Professional Publishing, 2015, 332.

(39) Brinker, C. J. Hydrolysis And Condensation Of Silicates: Effects On Structure. *J. Non-Cryst. Solids* **1988**, *100*, 31−50.

(40) Stathi, P.; Deligiannakis, Y.; Louloudi, M. Co-Catalytic Enhancement of H_2 Production by SiO_2 Nanoparticles. *Catal. Today* **2015**, *242*, 146−152.

(41) Papastergiou, M.; Stamatis, A.; Simaioforidou, A.; Louloudi, M. Bio-Inspired Mn-Catalysts Immobilized on Silica Surface: The Influence of the Ligand Synthesis on Catalytic Behavior. *Catal. Commun.* **2018**, *108*, 33−40.

(42) Capeletti, L. B.; Baibich, I. M.; Butler, I. S.; Dos Santos, J. H. Z. Infrared and Raman Spectroscopic Characterization of Some Organic Substituted Hybrid Silicas. *Spectrochim. Acta, Part A* **2014**, *133*, 619−625.

(43) Kalampounias, A. G. IR and Raman Spectroscopic Studies of Sol − Gel Derived Alkaline-Earth. *High Temp.* **2011**, *34*, 299−303.

(44) Capeletti, L.; Zimnoch, J. Fourier Transform Infrared and Raman Characterization of Silica-Based Materials In *Applications of Molecular Spectroscopy to Current Research in the Chemical and Biological Sciences*, edited by Stauffer, M. London: IntechOpen, 2016. DOI: 10.5772/64477.

(45) Singappuli-Arachchige, D.; Slowing, I. I. Control of Interfacial pH in Mesoporous Silica Nanoparticles via Surface Functionalization. *J. Chem. Phys.* **2020**, *152*, No. 034703.

(46) Júnior, J. A. A.; Baldo, J. B. The Behavior of Zeta Potential of Silica Suspensions. *New J. Glass Ceram.* **2014**, *04*, 29−37.

(47) Eftekhari, M.; Schwarzenberger, K.; Javadi, A.; Eckert, K. The Influence of Negatively Charged Silica Nanoparticles on the Surface Properties of Anionic Surfactants: Electrostatic Repulsion or the Effect of Ionic Strength? *Phys. Chem. Chem. Phys.* **2020**, *22*, 2238−2248.

(48) Murdock, R. C.; Braydich-Stolle, L.; Schrand, A. M.; Schlager, J. J.; Hussain, S. M. Characterization of Nanomaterial Dispersion in Solution Prior to in Vitro Exposure Using Dynamic Light Scattering Technique. *Toxicol. Sci.* **2008**, *101*, 239−253.

(49) Nel, A.; Xia, T.; Mädler, L.; Li, N. Toxic Potential of Materials at the Nanolevel. *Science* **2006**, *311*, 622−627.

(50) Efthimiou, I.; Kalamaras, G.; Papavasileiou, K.; Anastasi-Papathanasi, N.; Georgiou, Y.; Dailianis, S.; Deligiannakis, Y.; Vlastos, D. ZnO, Ag and ZnO-Ag Nanoparticles Exhibit Differential Modes of Toxic and Oxidative Action in Hemocytes of Mussel Mytilus Galloprovincialis. *Sci. Total Environ.* **2021**, *767*, No. 144699.